Ultimate bunch length and emittance performance of an MeV ultrafast electron diffraction apparatus with a dc gun and a multicavity superconducting rf linac

A. Bartnik,[1] C. Gulliford,[3] G. H. Hoffstaetter,[1,2] and J. Maxson[1]
[1]*Cornell University, Ithaca, New York 14850, USA*
[2]*Brookhaven National Laboratory, Upton, New York 14850, USA*
[3]*Xelera, Ithaca, New York 14850, USA*

(Received 29 September 2021; accepted 6 September 2022; published 22 September 2022)

We present the design of a high repetition rate MeV energy ultrafast electron diffraction instrument based on a dc photoelectron gun and an superconducting rf (SRF) linac with multiple independently controlled accelerating and bunching cavities. The design is based on the existing Cornell photoinjector, which can readily be applied to the presented findings. Using particle tracking simulations in conjunction with multiobjective genetic algorithm optimization, we explore the smallest bunch lengths, emittance, and probe spot sizes achievable. We present results for both stroboscopic conditions (with single electrons per pulse) and with 10^5 electrons/bunch which may be suitable for single-shot diffraction images. In the stroboscopic case, the flexibility provided by the many-cavity bunching and acceleration allows for longitudinal phase space linearization without a higher harmonic field, providing sub-fs bunch lengths at the sample. Given low emittance photoemission conditions, these small bunch lengths can be maintained with probe transverse sizes at the single micron scale and below. In the case of 10^5 electrons per pulse, we simulate state-of-the-art 5D brightness conditions: rms bunch lengths of 10 fs with 3-nm normalized emittances, while now permitting repetition rates as high as 1.3 GHz. Finally, to aid in the design of new SRF-based ultrafast electron diffraction machines, we simulate the trade-off between the number of cavities used and achievable bunch length and emittance.

DOI: 10.1103/PhysRevAccelBeams.25.093401

I. INTRODUCTION

Electron diffraction [1,2] and microscopy [3] with subpicosecond temporal resolution have become invaluable tools for the discovery and characterization of a wide variety of phenomena that occur far from static equilibrium. These include phase transitions, which have shown dramatic changes in material lattice symmetry [4], charge ordering [5,6], and electrical conductivity [7,8], and may be a useful tool for the continued study of light-induced superconductivity [9–11].

Ultrafast electron diffraction (UED) has been performed with a variety of electron accelerator technology ranging from tabletop keV sources to high brightness photoinjectors with MeV energies. While more complex to build than their keV counterparts, MeV energies provide several advantages. The higher energy relativistically suppresses the space charge interaction [12], allowing for higher density bunches and/or more flexible electron optics set points. In terms of diffraction performance, MeV electrons have a deeper penetration into materials allowing for thicker samples, and furthermore, the flatter Ewald sphere of MeV electrons permits more efficient scattering into higher order Bragg peaks [13].

MeV UED was pioneered with high brightness normal conducting rf photoguns [14–17], which can provide very high accelerating fields (∼100 MV/m) but at low repetition rates (hundreds of Hz or less). Recently, several MeV UED systems have been designed and constructed which are capable of operating at MHz repetition rates [18,19], which is very useful for gas phase samples or for investigating solid state samples with nondestructive pump excitation energy density [20]. dc and cw rf sources usually operate with lower photocathode gradients (up to ≈10 MV/m for dc sources and a few 10 s of MV/m for cw rf sources), these systems still retain the capability to generate a sufficient charge for single-shot diffraction pattern acquisition and furthermore have the ability to run in stroboscopic mode with charges as low as one electron per pulse [21].

In this work, we present the design of an MeV-UED system based on a dc photoelectron gun and superconducting rf linac booster. This system is based on the Cornell

superconducting rf (SRF) injector installed at the CBETA accelerator, originally designed for the generation of 100 pC-scale bunches for high repetition rate light source applications [22]. It is capable of any repetition rate which is an integer divisor of 1.3 GHz. While the source gradient is less than rf guns, the injector is equipped with an atypically large number of transverse focusing elements (three solenoids) and independently controlled 1.3 GHz rf cavities (five SRF cavities and one normal conducting cavity). The larger number of elements is due to the more detailed nature of emittance compensation in this dc-gun driven injector [23,24]. In the UED regime, however, the large number of degrees of freedom provides versatility for very high performance both in the stroboscopic (space charge free) regime and in the single shot (significant space charge) regime.

While having a lower gradient, the use of a dc gun does permit significant flexibility in the choice of photocathode and mode of illumination: high quantum efficiency, low emittance photocathodes can be used in both reflection mode and transmission mode (illumination from behind) [25]. Transmission mode photocathodes with built-in optical focusing can yield single digit micron initial source sizes [26]. We will demonstrate that in the space charge free regime, this can lead to the production of probe sizes below 1 μm, which would be advantageous to study the dynamics of materials near grain boundaries or domains [27]. In the single-shot regime, we will show that in conjunction with collimating apertures, a novel focusing scheme achieves very high quality emittance compensation for the central core of the beam composing 40% of particles, for a resulting beam size of 5 μm (rms), which is well tuned for diffraction from small flakes of advanced materials [28].

In the longitudinal dimension, we make use of the fact that MeV UED requires much lower energy than the 15-MeV maximum energy of the injector, and we may therefore use several of the SRF cavities for bunch length compression. In practice, we use a genetic optimization algorithm to choose the phases and amplitudes of the cavities appropriately for optimal bunching. In the zero space charge case, we find that bunching and acceleration are distributed across the six cavities in a way that produces a linearizing effect similar to that reported in Ref. [29]. In this regime, we will show that the ultimate bunch length can be limited by time-of-flight differences arising from transverse size and transverse momentum spread.

The minimum bunch lengths achievable in simulation without space charge are well below 1 fs and in the case of single-shot space charge conditions, between 5 and 20 fs (rms). However, in practice, the ultimate time resolution of the instrument may be limited by time of arrival fluctuations determined by phase and amplitude fluctuations of the accelerating fields. We conclude this work with a parametric study of the sensitivity of the device to these fluctuations.

II. INSTRUMENT LAYOUT

The layout of the injector is shown in Fig. 1 and remains largely unchanged from that in previous works [22,30,31]. It begins with a 400 kV dc gun, followed by a short section that includes two emittance compensating solenoids and a normal conducting rf bunching cavity. Following that is the injector cryomodule (ICM), containing five 2-cell SRF acceleration cavities, each with independent phase and amplitude control, capable of producing a net energy gain up to 15 MeV. As currently installed, the ICM is followed by a four-quadrupole telescope section, which we have modified for this design work. In the design presented here, we replace the final two quadrupole magnets with an additional solenoid and the UED sample chamber. Most of the focusing onto the sample is provided by this solenoid, while any asymmetry in the beam induced by the input couplers to the SRF cavities (which are included in our field model) is canceled by the remaining two quadrupoles.

This provides six independent rf phase and amplitude knobs, along with three solenoid focusing lenses for matching, emittance compensation, and final focusing. The photocathode can be driven by the laser from behind, in transmission mode. This allows for the option to include on-board focusing near the photoemission surface. Analytic estimates and experimental evidence show that this can enable initial Gaussian rms beam sizes down to approximately 2 μm [26]. In optimization, we require the initial Gaussian width to be $\sigma_x > 2$ μm, and we also require that the initial laser pulse length $\sigma_t > 1$ ps, which is sufficiently long compared to the expected photocathode response time given the nanometer-scale thickness of high quantum efficiency photocathodes [32]. Above those constraints, spot size and bunch length are considered free parameters to be optimized as needed. Final energy is allowed to vary, and all optima shown below lie within 4 and 5 MeV total energy.

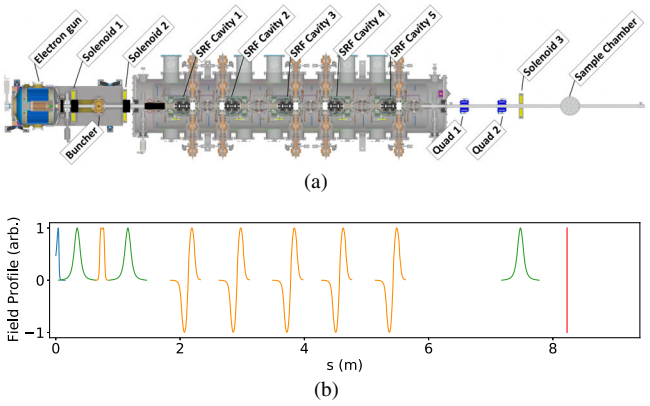

FIG. 1. (a) 3D model of the apparatus. (b) Electric and magnetic field profiles along the beamline. The dc gun field is shown in blue, solenoid fields in green, rf cavities in orange, and the sample location is shown via a red line.

III. PARAMETER OPTIMIZATION

In the following section, we will limit ourselves to optimization of the beamline's single-bunch performance, deferring a discussion of the effects of multibunch stability until the following section. All of our simulation work is performed with General Particle Tracer (GPT) [33,34], using a Multiobjective Genetic Algorithm (MOGA) optimization [22,35,36]. Although the gun, buncher, and solenoid field maps are cylindrically symmetric, the SRF cavity field maps included the effects of the input couplers and are fully 3D. Two sets of optimizations were performed, one without space charge which models single electron/pulse conditions, and one with 10^5 electron/pulse to approximate conditions for single-shot diffraction. All optimizations with 10^5 electron/pulse were performed at a reduced number of simulated macroparticles of 5000, which we found to be sufficient to produce the correct physical trends in the optimized Pareto fronts. After optimizing, select cases were recalculated with 250,000 macroparticles to verify convergence. Typically, the transverse emittance was reduced and the bunch length remained nearly identical after recalculation.

A. Stroboscopic mode: One electron per pulse

Even when including 3D effects in the fields (aberrations), at zero space charge and with micron-scale initial spot sizes, the simulation predicts full emittance preservation, and the emittance is therefore no longer an optimization objective. The emittance is set by initial conditions such as the mean transverse energy (MTE) of the photoemission process and the incident laser spot size [37]. In all following simulations, the cathode MTE was set to 35 meV, assuming near threshold illumination of alkali antimonide photocathodes, which have been the standard for this electron gun [38]. Optimizing the machine parameters, in this case, is much simpler, as there is no need for emittance compensation, and only the bunch's final transverse and longitudinal size need to be optimized. In practice, emittance evolution without space charge effects will be determined by field quality and is outside the scope of this work. Nonetheless, we see an important trade-off between final spot size and bunch length described below.

Without the need to compensate for transverse emittance, cavity parameters may vary freely while maintaining the desired final energy. This allows advanced longitudinal phase space manipulation techniques to be performed to mitigate the negative effects of nonlinear time of flight- and cavity-induced phase space curvature without higher harmonic fields, similar to what was derived in [29]. Extremely short bunch lengths are possible since the phase space can be linearized to high order at the sample plane. We find that the bunch length is then not limited by rf curvature but rather by the coupling of the time of flight to transverse momentum. This coupling of transverse and longitudinal coordinates has been well studied for sub-femtosecond beams [39–41], and here we find that it is this phenomenon that sets the trade-off between ultimate bunch length and spot size.

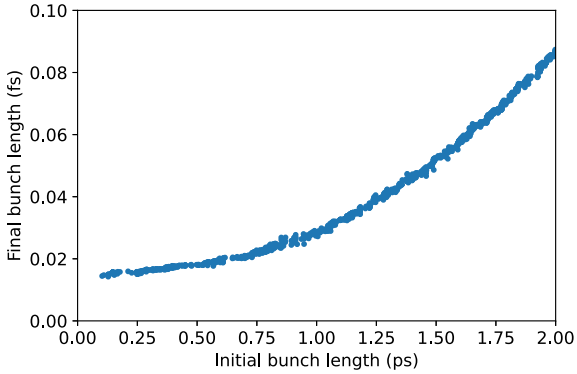

FIG. 2. Dependence of achievable bunch length on initial bunch length at the cathode. An initial transverse spot size of 2 μm was used for these simulations.

Because our beam begins with a tight focus at the cathode, the downstream trajectory of each emitted electron is determined almost entirely by its initial transverse momentum. Larger initial momenta will produce trajectories that deviate further from the transverse center, causing a longer path length to the sample. Thus, for a fixed set of machine optics in this apparatus, the minimal bunch length in the sample plane is primarily a function of the cathode's MTE and depends only weakly on the initial longitudinal size when below ≈1 ps, as shown in Fig. 2.

The final transverse beam size is determined by the emittance of the beam and by how strongly the beam is focused on the sample. As the emittance increases, achieving a given final beam width will require stronger focusing, which is only possible with larger beam widths at the focusing optics. But, larger widths during beam transport also produce larger spreads in time of flight. That is, for a given final beam width, a larger emittance will result in a longer bunch length. This is opposite to the typical behavior of space charge dominated beams. In addition, for a constant emittance, there will be a trade-off between beam size and bunch length.

We can get insight into both of these trends by looking at the spread in path lengths near the sample. At the sample location, if the emittance and beam size are known, then the momentum spread can be directly determined as $\sigma_{p_x} = mc\epsilon_n/\sigma_x$. For each individual electron, the time of flight from the last focusing magnet to the sample is $\Delta t_f = L/v_z = Lm\gamma/\sqrt{p^2 - p_x^2 - p_y^2} \approx L\frac{m\gamma}{p}(1+\frac{1}{2})\frac{p_x^2+p_y^2}{p^2}$, with an rms spread of $\sigma_{t_f} = L\frac{m\gamma}{\sqrt{2}p^3}\sqrt{\langle p_x^4\rangle - \sigma_{p_x}^4}$. Assuming a Gaussian spread in momenta, and cylindrical symmetry, this produces a spread in time-of-flights back to the location of the final focusing magnet given by

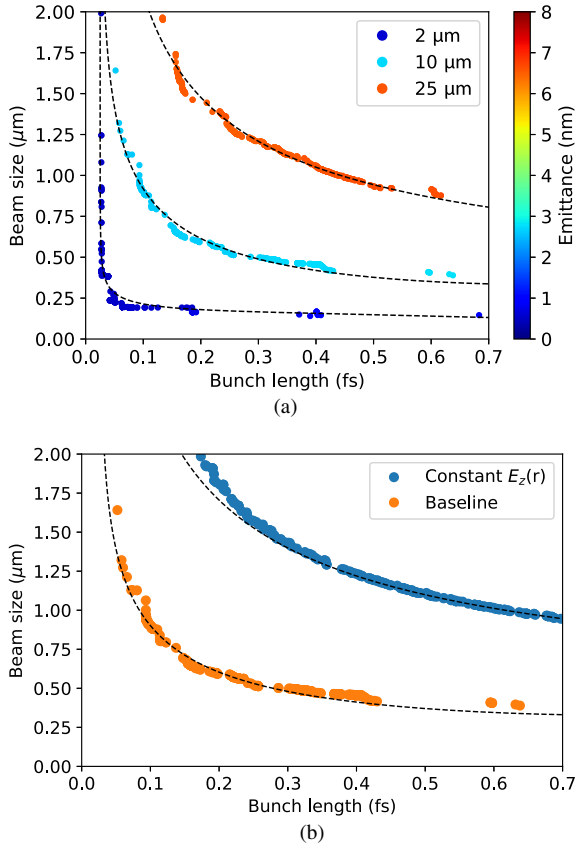

FIG. 3. (a) Dependence of achievable bunch length on final beam size in the absence of space charge forces for three different initial laser sizes: 2, 10, and 25 μm (dots), compared to a simple model (lines). Here the MTE is 35 meV, and so these laser sizes correspond to normalized source emittances of 0.5, 2.6, and 6.5 nm, respectively. (b) Comparison between optimizations using the default cavity field maps and ones without radial dependence of the accelerating fields. In both cases, an initial laser size of 10 μm was used.

$$\sigma_{t_f} = \frac{L\epsilon_n^2}{\beta c(\gamma\beta)^2\sigma_x^2} \tag{1}$$

where L is the drift length from the lens to the sample, ϵ_n is the normalized beam emittance, and σ_x is the beam size at the sample. This only describes the spread in time of flights induced by the last focusing magnet, though we will still apply this model to our optimizations with the addition of an overall scale factor. Figure 3(a) shows the optimal Pareto fronts from the MOGA optimizations for three different choices of initial laser size, along with this model scaled by a factor of 0.5. We interpret this scale factor being less than 1.0 as the optimization of finding a way to compensate for most of the spread in path lengths.

We believe that the primary mechanism that is used to mitigate this is the dependence of the cavity accelerating field on radius. It is generally true [42] that the energy gain experienced by a particle in a cavity on crest increases

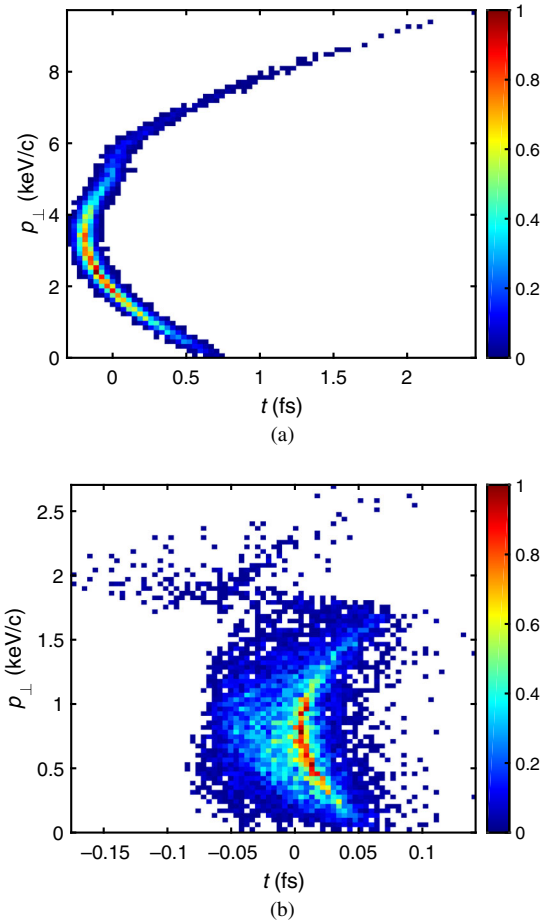

FIG. 4. Correlation between time and transverse momentum at the sample location. Examples are shown for both (a) typical and (b) minimal bunch lengths.

quadratically with particle radius $E \propto 1 + (\pi r)^2/(\beta\gamma\lambda)^2$. Thus, particles at larger radii that have taken longer to arrive at the cavity will be accelerated slightly more, compensating for their path length. To verify that this was the primary mechanism, we separately optimized the same beamline using field maps without any radial dependence in the accelerating field E_z and only a linear focusing in the radial field E_r, which is achieved in GPT by supplying a 1D on-axis field map and using its built-in off-axis expansion. As shown in Fig. 3(b), the Pareto front is significantly worse and is now best fit to the analytic trend with a scale factor of 2.1, implying that little or no compensation of the path length has occurred.

To illustrate the details of this effect, the correlation between arrival time and transverse momentum is shown in Fig. 4. For most of the optimal points on the front, the beam is similar to Fig 4(a), where the linear correlation has been removed, but a large quadratic correlation remains. But for the smallest bunch lengths, where σ_{p_x} at the sample is small, this remaining correlation is no longer the limiting factor as in Fig. 4(b). For this minimal bunch length case,

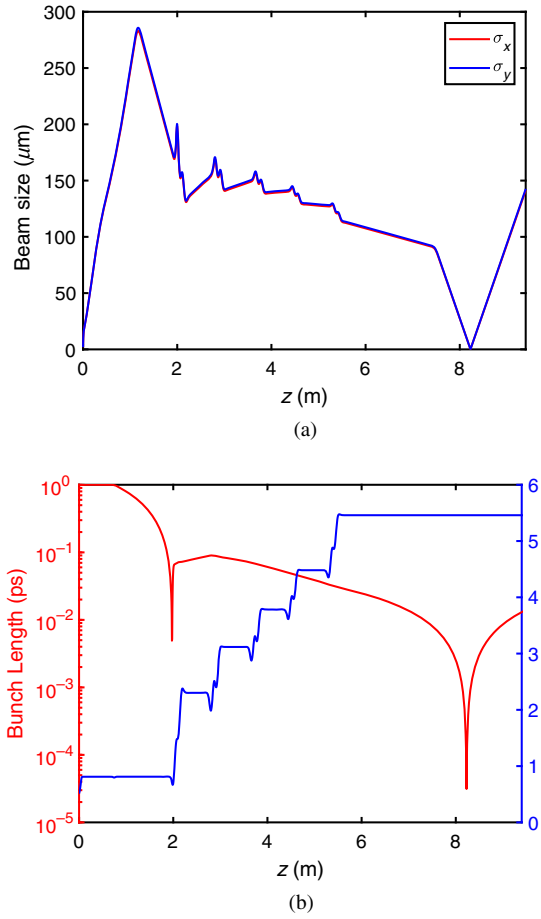

FIG. 5. (a) Beam width and (b) bunch length and energy throughout the injector at near zero charge for an example solution on the Pareto front. The sample (and clipping aperture) is located at $z = 8.228$ m.

we plot the transverse beam size, bunch length, and energy in Fig. 5.

It must be noted that the final achievable bunch lengths are in the range of a few femtoseconds down to <100 attoseconds (rms), which suggests multicavity injectors of this type as a promising route to generate high repetition rate, isolated attosecond electron pulses. However, in practice with the current state of the art, we will show below that UED temporal resolution will be limited by the phase and amplitude stability of the accelerating fields; time-stamping techniques [43] with sufficient precision would be needed to overcome this limitation.

B. Single-shot mode: 10^5 electrons per pulse

At a charge of 16 fC, with 10^5 electrons, space charge becomes the dominant effect in transverse and longitudinal dynamics and careful emittance compensation is required. Optimizations were performed to determine to what extent these effects can be mitigated in this apparatus, which has a much smaller source accelerating gradient (~5 MV/m) than other MeV UED machines which are based on rf guns. MOGA optimizations were started with three objectives: beam size, emittance, and bunch length. Once roughly converged, the beam size objective was replaced with a constraint ($\sigma_x < 30$ μm), and the MOGA was continued with only two objectives. This beam size constraint was chosen so that even with significant space charge, diffraction from most samples can be achieved. In practice, the optimizer would tend to aggressively focus the beam and was typically well under the 30 μm beam size constraint. This is atypical of space charge optimizations, and we believe it was due to our use of an adjustable aperture, as explained below.

An aperture directly before the sample location is a practical way to force the size of the electron beam to be compatible with a given sample size [44]. In addition, if one emits more charge than necessary, the final sample pinhole can be used to improve the transverse emittance performance of the device by selecting only the beam's dense core, which has experienced a more linear space charge force overall. To exploit this, we allowed the optimization to begin with a larger charge of 40 fC and then subsequently clip back to 16 fC at the sample location with an adjustable circular aperture. We chose that value of initial charge because we found that increasing the initial charge above 40 fC produced only marginal improvement while requiring longer simulation times. In each simulation, the radius of the aperture was chosen to produce precisely the target charge of 16 fC, with typical aperture sizes ~10 μm diameter. Apertures of this size appropriate for few-MeV level electron beams can be manufactured via laser machining of thin metal films. The optimizer found that the effect of strong focusing would be to produce a bright central beam core, surrounded by a large diffuse halo. Without an aperture, this halo would ruin the beam's emittance and brightness, but with an aperture, it was an overall improvement. As a result, the optimizer would choose to focus strongly on small apertures.

Apertures are commonly used in MeV UED [45–47]. Laser-machined apertures at the 10 μm scale can be made with thicknesses approaching 100 μm, which is sufficient to strongly scatter a few MeV beams [48]. In typical UED practice, the data are presented as a diffraction difference pattern between unexcited and pumped sample conditions. If the aperture-induced scattering is well sampled by the detector, it will not affect the diffraction difference data.

The optimization results with and without using a sample-plane aperture are shown in Fig. 6(a). For most bunch lengths, the emittance is significantly reduced by the aperture, although the minimum achievable bunch length is slightly worse due to the requirement of starting with a larger initial charge, and due to transverse/longitudinal spatial correlations present in the bunch prior to the aperture. To determine the impact of the photoemission

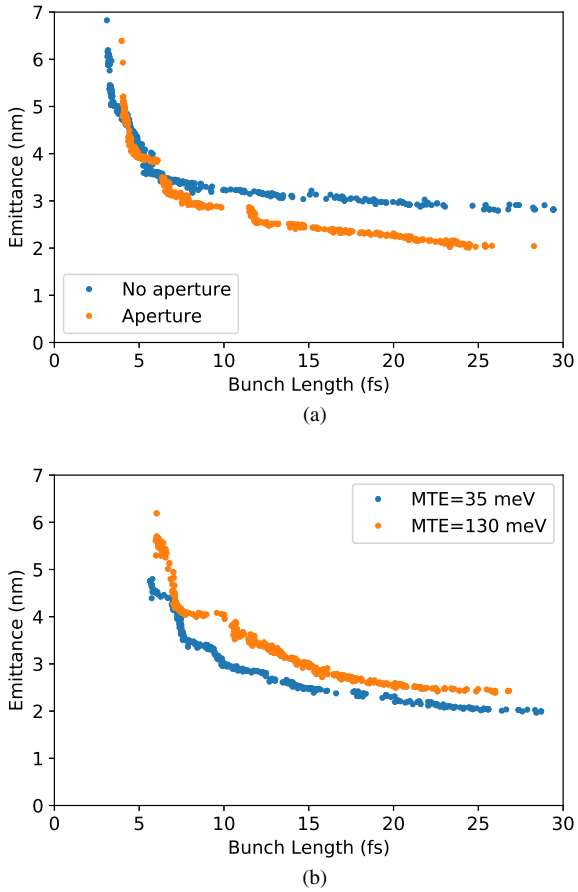

FIG. 6. (a) Influence of collimation on the achievable bunch length and emittance with a final bunch charge of 16 fC. (b) Effects of the cathode mean transverse energy (MTE) on the final bunch length and emittance at the same charge.

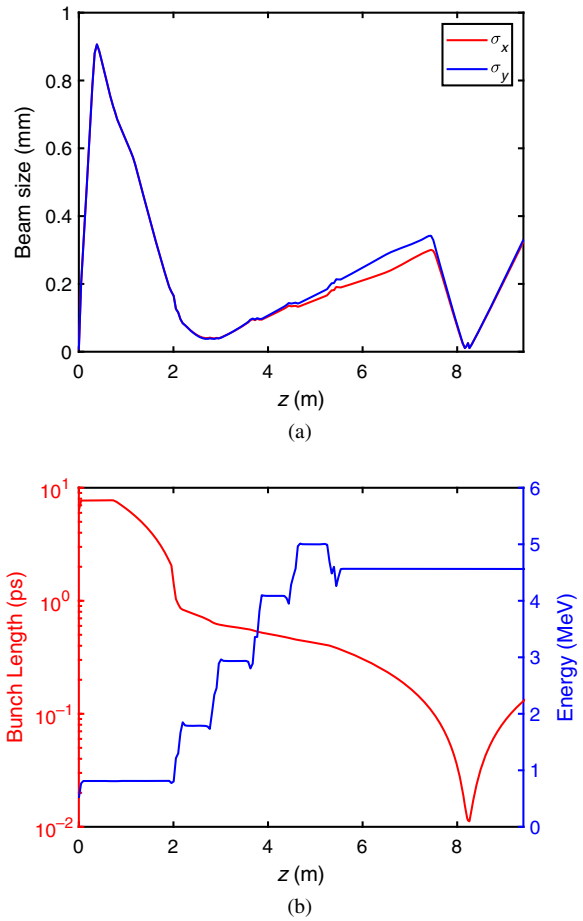

FIG. 7. (a) Beam width and (b) bunch length and energy throughout the injector at a final charge of 10^5 electrons/pulse. After the sample (and clipping) aperture at $z = 8.228$ m, the bunch had an emittance of 2.6 nm, beam width of 5 μm, and bunch length of 10 fs.

MTE on the final properties of the beam, simulations were performed at both an MTE of 35 and 130 meV, as shown in Fig. 6(b). The latter is typical for multialkali cathodes when illuminated with green light, which is often easier to obtain via doubling of commercially available Yb-based high repetition rate lasers, while the former requires a laser tuned to near-threshold illumination. Experimentally reaching 35 meV at the particle densities simulated here is potentially challenging due to two effects: disorder-induced heating (DIH) and the onset of multiphoton photoemission. We do not expect DIH to be a significant effect, as the particle density at the cathode only reaches $\approx 2 \times 10^{18}$ m^{-3}, leading to heating of only ≈ 1 meV [49]. On the other hand, multiphoton photoemission may be a significant effect, depending on the cathode's quantum efficiency. If a significant fraction of the bunch's electrons is excited from more than a single photon, there would be two populations of electrons: those with low MTE (singly excited electrons) and those with high MTE (doubly excited electrons). In momentum space, this distribution will look like a sharply peaked Gaussian atop a wider one. Therefore, even if this effect becomes important, it may be possible to eliminate the contribution of multiphoton photoemission via apertures. Regardless, it is valuable to model the effect of lower MTE to judge the potential for improvement.

To look more closely at the dynamics of the bunch, an example was chosen from the 130 meV MTE Pareto front and reevaluated at higher simulation accuracy settings. As is typical for space charge simulations, the higher accuracy slightly reduces the final beam emittance from the value shown in the Pareto front, so that an emittance of 3 nm is achievable at a bunch length of 10 fs. Beam width and bunch length throughout the beamline are shown in Fig. 7, and example particle distributions are shown in Fig. 8 both before and after the final clipping aperture. Because of the correlation between transverse position and arrival time, clipping occurs in both transverse and longitudinal planes. The aperture improves not only the emittance but also the transverse brightness of the electron bunch $B = Q/\epsilon_x\epsilon_y$. In Fig. 9, the radius of the aperture is varied and the brightness of the remaining particles is shown to approach a constant value when only the core of the beam remains. The space

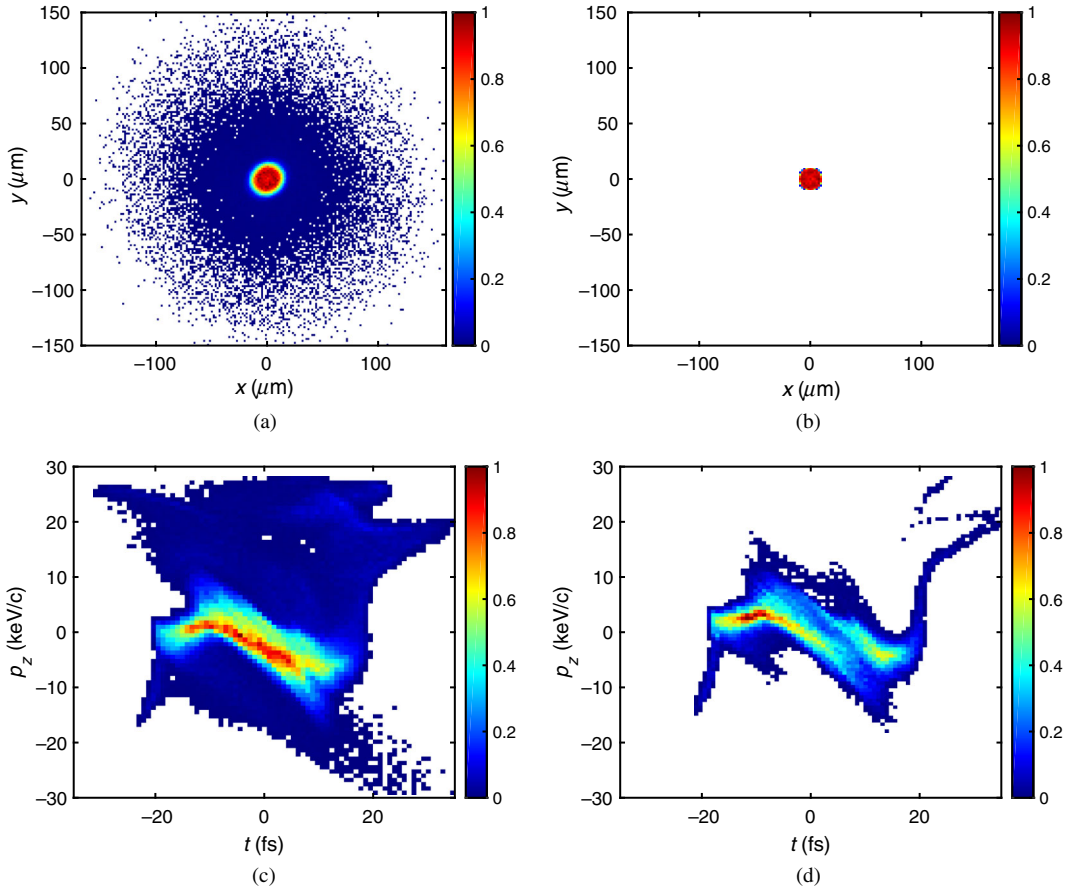

FIG. 8. Bunch transverse distribution and longitudinal phase space before and after going through the aperture at the sample location at a final charge of 10^5 electrons/pulse. After the aperture, the bunch had an emittance of 2.6 nm, beam width of 5 μm, and bunch length of 10 fs. (a) Transverse distribution before aperture. (b) Transverse distribution after aperture. (c) Longitudinal phase space before aperture. (d) Longitudinal phase space after aperture.

charge dynamics of this focusing scheme is more general than this application alone and justifies a detailed analysis in future work. We note that the 5D brightness simulation, with bunch length and emittance in the range of 10 fs and 2–3 nm (depending on MTE), exceeds the experimental state of the art [28,50,51] and naturally permits operation at a very high repetition rate.

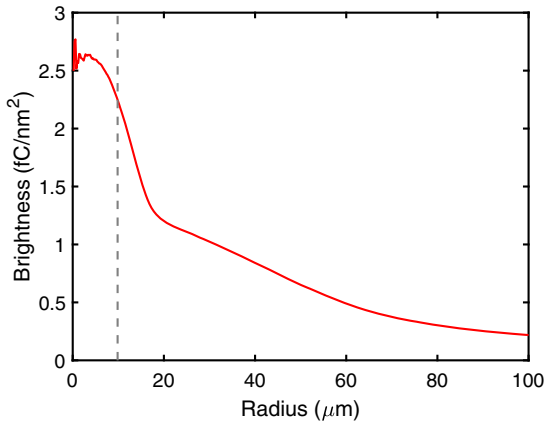

FIG. 9. Dependence of transverse brightness on the clipping aperture's radius. The dashed line indicates the radius used in optimization.

IV. TIME OF ARRIVAL VARIATION DUE TO PHASE AND AMPLITUDE STABILITY

While the design choice of many independent cavity phases and amplitudes provides several advantages, for a given achievable phase and amplitude stability, more cavities can lead to a worse time of arrival stability. Without time-stamping techniques to determine post-facto the arrival time of the bunch, this time of arrival variation directly translates to reduced temporal resolution. We define a figure of merit for the temporal resolution of any measurement which is a combination of the bunch length σ_t and the arrival time stability σ_{t_0}: $\sigma_{t,\mathrm{res}} = \sqrt{\sigma_t^2 + \sigma_{t_0}^2}$. This intentionally neglects the effect of the pump laser stability. Because of the large longitudinal compression of our beamline, pump laser stability will be nearly completely uncorrelated to the e-beam, and the true experimental resolution would require this additional effect to be added

TABLE I. Sensitivity to machine parameters.

Parameter	Setting	Stability	Units	σ_{t_0} (fs)
Gun amplitude	300	0.03	kV	2.3
Buncher amplitude	26	0.001	kV	0.5
Cavity 1 amplitude	1150	0.03	kV	1.0
Cavity 2 amplitude	1170	0.03	kV	1.0
Cavity 3 amplitude	1590	0.03	kV	0.5
Cavity 4 amplitude	1290	0.03	kV	0.4
Cavity 5 amplitude	1250	0.03	kV	0.2
Buncher phase	−90	0.01	deg.	0.8
Cavity 1 phase	−1	0.01	deg.	0.7
Cavity 2 phase	−9	0.01	deg.	2.7
Cavity 3 phase	−51	0.01	deg.	6.5
Cavity 4 phase	−45	0.01	deg.	6.2
Cavity 5 phase	−104	0.01	deg.	4.7
Total				13

in quadrature to the figure of merit. Importantly, in UED machines that do not include such strong longitudinal compression, the electron bunches would naturally follow the jitter of the cathode/pump laser, and this effect would be greatly reduced. Thus, in order to benefit from the optimizations presented here, much stronger requirements are placed on the laser system, or it will likely become the dominant limiting source of machine resolution. Regardless, the methods used to reduce laser arrival jitter are beyond the scope of this work and will not be discussed here.

To determine σ_{t_0}, we use previously experimentally measured stability of each machine component [52] and performed many simulations with settings chosen randomly from the measured distributions. In addition, we also performed simulations that only allowed a single machine parameter to vary, in order to see which parameters individually mattered the most. Using the same example machine setting as in Figs. 7–9, Table I shows the measured stability of each machine parameter, and the individual contribution of it toward arrival time stability. The achievable arrival time stability is around 13 fs, with the most significant contributions coming from the phase of the off-crest cavities, which is to be expected. As a result, the bunch length and arrival time stability will contribute nearly equally to the total temporal resolution in this case.

It is not clear from that single example case to what degree each of the SRF cavities is required in order to reach that level of performance. To better understand that, we performed additional MOGA optimizations, this time optimizing the temporal resolution (including stability and bunch length). We did this 5 times, each time reducing the number of SRF cavities by one while keeping the rest of the beamline unchanged. The beam energy used by the optimizer remained mostly unchanged for these simulations at roughly 4 MeV, though in the case of a single remaining cavity, the final beam energy was limited to a maximum of 3 MeV. In Fig. 10(a), the Pareto fronts of these optimizations are shown. In Fig. 10(b), a cut along these fronts at an emittance of 4 nm is shown, and both the temporal resolution and the bunch length are plotted. From these plots, it is clear that in single-shot mode at least three independent SRF cavities are needed for best performance, and it is primarily the bunch length that limits the temporal resolution below that number. However, given the ultimate single electron performance of this machine is well below 1 fs, this mode of operation would require nondestructive high-precision time of arrival measurements for time stamping to circumvent the effects of machine stability.

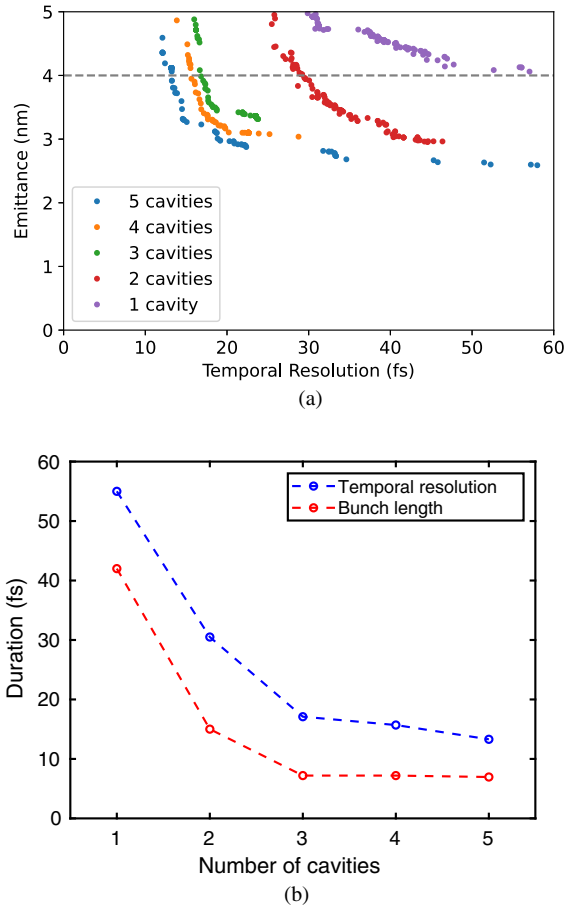

FIG. 10. (a) Trade-off between achievable temporal resolution and emittance for different numbers of SRF cavities. (b) Temporal resolution and bunch length for different numbers of SRF cavities at a constant emittance of 4 nm.

V. CONCLUSION

We have presented a design for a flexible, high repetition rate MeV ultrafast electron diffraction apparatus based on the injector at Cornell University and have characterized its performance from the space charge-free stroboscopic regime to the space charge–dominated regime pertinent to single-shot diffraction.

In the single electron per pulse regime, we find that the ultimate bunch length achievable in simulation is well below 1 fs rms, owing to the longitudinal phase space linearization that is possible using multiple accelerating and bunching cavities. In the case of very small spot sizes, the single electron/pulse bunch length is ultimately limited by transverse to longitudinal coupling. In practice, however, even state of the art rf synchronization produces time of arrival variations at the level of 10 fs rms or larger. We show that while the increased complexity of our rf system greatly reduces bunch length, it is unable to significantly reduce this arrival time instability. Considering the large gap between simulated bunch length performance and practical arrival time uncertainty, our work suggests that noninvasive time-stamping techniques with high temporal resolutions may be required to unlock attosecond MeV single electron pulses for experimental use.

With 10^5 electrons per pulse, we find that the use of a small collimating aperture enables the use of strong transverse focusing to generate a dense transverse core with a large halo, wherein the halo is ultimately removed by a pinhole. Ultimately, the system achieves 2–3 nm emittance (depending on photocathode MTE) and 10 fs rms pulse lengths; shorter pulses down to 5-fs rms are possible with 4–5 nm emittance.

Finally, we analyze the ultimate temporal resolution of the device accounting for both bunch length and time of arrival variations using the measured field stability values in the Cornell SRF photoinjector. We do this as a function of the number of accelerating cavities included in the cryomodule to aid in future designs. We find that at least three cavities are required for significant performance gains. With five cavities, we show that field stability has a minor impact on high charge performance, yielding a total temporal resolution of 14-fs rms.

ACKNOWLEDGMENTS

This work was supported by DOE Award No. DE-SC0021037 and No. DE-SC0020144.

[1] G. Mourou and S. Williamson, Picosecond electron diffraction, Appl. Phys. Lett. **41**, 44 (1982).
[2] G. Sciaini and R. Miller, Femtosecond electron diffraction: Heralding the era of atomically resolved dynamics, Rep. Prog. Phys. **74**, 096101 (2011).
[3] A. H. Zewail, 4D ultrafast electron diffraction, crystallography, and microscopy, Annu. Rev. Phys. Chem. **57**, 65 (2006).
[4] E. J. Sie *et al.*, An ultrafast symmetry switch in a Weyl semimetal, Nature (London) **565**, 61 (2019).
[5] S. Vogelgesang, G. Storeck, J. G. Horstmann, T. Diekmann, M. Sivis, S. Schramm, K. Rossnagel, S. Schäfer, and C. Ropers, Phase ordering of charge density waves traced by ultrafast low-energy electron diffraction, Nat. Phys. **14**, 184 (2018).
[6] A. Kogar *et al.*, Light-induced charge density wave in $LaTe_3$, Nat. Phys. **16**, 159 (2020).
[7] V. R. Morrison, R. P. Chatelain, K. L. Tiwari, A. Hendaoui, A. Bruhács, M. Chaker, and B. J. Siwick, A photoinduced metal-like phase of monoclinic VO_2 revealed by ultrafast electron diffraction, Science **346**, 445 (2014).
[8] M. R. Otto, L. P. R. de Cotret, D. A. Valverde-Chavez, K. L. Tiwari, N. Émond, M. Chaker, D. G. Cooke, and B. J. Siwick, How optical excitation controls the structure and properties of vanadium dioxide, Proc. Natl. Acad. Sci. U.S.A. **116**, 450 (2019).
[9] M. Budden, T. Gebert, M. Buzzi, G. Jotzu, E. Wang, T. Matsuyama, G. Meier, Y. Laplace, D. Pontiroli, M. Riccò, F. Schlawin, D. Jaksch, and A. Cavalleri, Evidence for metastable photo-induced superconductivity in K_3C_{60}, Nat. Phys. **17**, 611 (2021).
[10] D. Fausti, R. I. Tobey, N. Dean, S. Kaiser, A. Dienst, M. C. Hoffmann, S. Pyon, T. Takayama, H. Takagi, and A. Cavalleri, Light-induced superconductivity in a stripe-ordered cuprate, Science **331**, 189 (2011).
[11] M. Mitrano, A. Cantaluppi, D. Nicoletti, S. Kaiser, A. Perucchi, S. Lupi, P. D. Pietro, D. Pontiroli, M. Riccò, S. R. Clark, D. Jaksch, and A. Cavalleri, Possible light-induced superconductivity in K_3C_{60} at high temperature, Nature (London) **530**, 461 (2016).
[12] M. Reiser, *Theory and Design of Charged Particle Beams* (Wiley-VCH, New York, 2008).
[13] P. Zhu, Y. Zhu, Y. Hidaka, L. Wu, and J. Cao, Femtosecond time-resolved MeV electron diffraction, New J. Phys. **17**, 063004 (2015).
[14] F. Fu, S. Liu, P. Zhu, D. Xiang, J. Zhang, and J. Cao, High quality single shot ultrafast MeV electron diffraction from a photocathode radio-frequency gun, Rev. Sci. Instrum. **85**, 083701 (2014).
[15] R. Li, C. Tang, Y. Du, W. Huang, Q. Du, J. Shi, L. Yan, and X. Wang, Experimental demonstration of high quality MeV ultrafast electron diffraction, Rev. Sci. Instrum. **80**, 083303 (2009).
[16] S. P. Weathersby *et al.*, Mega-electron-volt ultrafast electron diffraction at SLAC National Accelerator Laboratory, Rev. Sci. Instrum. **86**, 073702 (2015).
[17] M. S. Gutierrez, H. A. Bender, and N. S. Wilcox, High quality single shot diffraction patterns using ultrashort megaelectron volt electron beams from a radio frequency photoinjector, Rev. Sci. Instrum. **81**, 013306 (2010).
[18] D. Filippetto and H. Qian, Design of a high-flux instrument for ultrafast electron diffraction and microscopy, J. Phys. B **49**, 104003 (2016).
[19] L. W. Feng, L. Lin, S. L. Huang, S. W. Quan, T. Jiang, P. F. Zhu, J. K. Hao, F. Zhu, F. Wang, F. Fu, R. Wang, L. Zhao, D. Xiang, and K. X. Liu, Ultrafast electron diffraction with megahertz MeV electron pulses from a superconducting radio-frequency photoinjector, Appl. Phys. Lett. **107**, 224101 (2015).
[20] S. Lahme, C. Kealhofer, F. Krausz, and P. Baum, Femtosecond single-electron diffraction, Struct. Dyn. **1**, 034303 (2014).

[21] F. Ji, D. B. Durham, A. M. Minor, P. Musumeci, J. G. Navarro, and D. Filippetto, Ultrafast relativistic electron nanoprobes, Commun. Phys. **2**, 54 (2019).

[22] C. Gulliford, A. Bartnik, I. Bazarov, L. Cultrera, J. Dobbins, B. Dunham, F. Gonzalez, S. Karkare, H. Lee, H. Li, Y. Li, X. Liu, J. Maxson, C. Nguyen, K. Smolenski, and Z. Zhao, Demonstration of low emittance in the Cornell energy recovery linac injector prototype, Phys. Rev. ST Accel. Beams **16**, 073401 (2013).

[23] L. Serafini and J. B. Rosenzweig, Envelope analysis of intense relativistic quasilaminar beams in rf photoinjectors: mA theory of emittance compensation, Phys. Rev. E **55**, 7565 (1997).

[24] I. V. Bazarov and C. K. Sinclair, Multivariate optimization of a high brightness dc gun photoinjector, Phys. Rev. ST Accel. Beams **8**, 034202 (2005).

[25] H. Lee, L. Cultrera, and I. Bazarov, Intrinsic emittance reduction in transmission mode photocathodes, Appl. Phys. Lett. **108**, 124105 (2016).

[26] C. Gerbig, A. Senftleben, S. Morgenstern, C. Sarpe, and T. Baumert, Spatio-temporal resolution studies on a highly compact ultrafast electron diffractometer, New J. Phys. **17**, 043050 (2015).

[27] A. Zong, X. Shen, A. Kogar, L. Ye, C. Marks, D. Chowdhury, T. Rohwer, B. Freelon, S. Weathersby, R. Li, J. Yang, J. Checkelsky, X. Wang, and N. Gedik, Ultrafast manipulation of mirror domain walls in a charge density wave, Sci. Adv. **4**, eaau5501 (2018).

[28] X. Shen, R. Li, U. Lundström, T. Lane, A. Reid, S. Weathersby, and X. Wang, Femtosecond mega-electron-volt electron microdiffraction, Ultramicroscopy **184**, 172 (2018).

[29] B. Zeitler, K. Floettmann, and F. Grüner, Linearization of the longitudinal phase space without higher harmonic field, Phys. Rev. ST Accel. Beams **18**, 120102 (2015).

[30] I. Bazarov *et al.*, The Cornell-BNL FFAG-ERL test accelerator: White paper, arXiv:1504.00588.

[31] B. Dunham *et al.*, Record high-average current from a high-brightness photoinjector, Appl. Phys. Lett. **102**, 034105 (2013).

[32] S. Karkare, L. Boulet, L. Cultrera, B. Dunham, X. Liu, W. Schaff, and I. Bazarov, Ultrabright and Ultrafast III–V Semiconductor Photocathodes, Phys. Rev. Lett. **112**, 097601 (2014).

[33] Pulsar website for gpt, http://www.pulsar.nl/gpt/ (2011).

[34] S. van der Geer, O. Luiten, M. de Loos, G. Pöplau, and U. van Rienen, 3d space-charge model for gpt simulations of high brightness electron bunches, in Institute of Physics Conference Series (2005), Vol. **175**, p. 101.

[35] C. Gulliford, A. Bartnik, I. Bazarov, B. Dunham, and L. Cultrera, Demonstration of cathode emittance dominated high bunch charge beams in a dc gun-based photoinjector, Appl. Phys. Lett. **106**, 094101 (2015).

[36] A. Bartnik, C. Gulliford, I. Bazarov, L. Cultera, and B. Dunham, Operational experience with nanocoulomb bunch charges in the Cornell photoinjector, Phys. Rev. ST Accel. Beams **18**, 083401 (2015).

[37] P. Musumeci, J. G. Navarro, J. Rosenzweig, L. Cultrera, I. Bazarov, J. Maxson, S. Karkare, and H. Padmore, Advances in bright electron sources, Nucl. Instrum. Methods Phys. Res., Sect. A **907**, 209 (2018).

[38] J. Maxson, L. Cultrera, C. Gulliford, and I. Bazarov, Measurement of the tradeoff between intrinsic emittance and quantum efficiency from a NaKSb photocathode near threshold, Appl. Phys. Lett. **106**, 234102 (2015).

[39] M. De Loos, S. van Der Geer, Y. Saveliev, V. Pavlov, A. Reitsma, S. Wiggins, J. Rodier, T. Garvey, and D. Jaroszynski, Radial bunch compression: Path-length compensation in an rf photoinjector with a curved cathode, Phys. Rev. ST Accel. Beams **9**, 084201 (2006).

[40] K. Floettmann, Generation of sub-fs electron beams at few-MeV energies, Nucl. Instrum. Methods Phys. Res., Sect. A **740**, 34 (2014).

[41] C. Weninger and P. Baum, Temporal distortions in magnetic lenses, Ultramicroscopy **113**, 145 (2012).

[42] C. Duncan, D. Muller, and J. Maxson, Lossless Monochromation for Electron Microscopy with Pulsed Photoemission Sources and Radio-Frequency Cavities, Phys. Rev. Applied **14**, 014060 (2020).

[43] L. Zhao, J. Wu, Z. Wang, H. Tang, X. Zou, T. Jiang, P. Zhu, D. Xiang, and J. Zhang, Non-invasive time-sorting in radio-frequency compressed ultrafast electron diffraction, arXiv:2105.03563.

[44] W. H. Li, C. J. R. Duncan, M. B. Andorf, A. C. Bartnik, E. Bianco, L. Cultrera, A. Galdi, M. Gordon, M. Kaemingk, C. A. Pennington, L. F. Kourkoutis, I. V. Bazarov, and J. M. Maxson, A kiloelectron-volt ultrafast electron microdiffraction apparatus using low emittance semiconductor photocathodes, Struct. Dyn. **9**, 024302 (2022).

[45] P. Musumeci, J. T. Moody, C. M. Scoby, M. S. Gutierrez, H. A. Bender, and N. S. Wilcox, High quality single shot diffraction patterns using ultrashort megaelectron volt electron beams from a radio frequency photoinjector, Rev. Sci. Instrum. **81**, 013306 (2010).

[46] S. P. Weathersby *et al.*, Mega-electron-volt ultrafast electron diffraction at SLAC National Accelerator Laboratory, Rev. Sci. Instrum. **86**, 073702 (2015).

[47] F. Ji, D. B. Durham, A. M. Minor, P. Musumeci, J. G. Navarro, and D. Filippetto, Ultrafast relativistic electron nanoprobes, Commun. Phys. **2**, 54 (2019).

[48] R. K. Li, K. G. Roberts, C. M. Scoby, H. To, and P. Musumeci, Nanometer emittance ultralow charge beams from rf photoinjectors, Phys. Rev. ST Accel. Beams **15**, 090702 (2012).

[49] M. Gordon, S. B. van der Geer, J. Maxson, and Y.-K. Kim, Point-to-point Coulomb effects in high brightness photoelectron beam lines for ultrafast electron diffraction, Phys. Rev. Accel. Beams **24**, 084202 (2021).

[50] J. Maxson, D. Cesar, G. Calmasini, A. Ody, P. Musumeci, and D. Alesini, Direct Measurement of Sub-10 fs Relativistic Electron Beams with Ultralow Emittance, Phys. Rev. Lett. **118**, 154802 (2017).

[51] P. Denham and P. Musumeci, Analytical scaling laws for radiofrequency based pulse compression in ultrafast electron diffraction beamlines, arXiv:2106.02102.

[52] M. Liepe, S. Belomestnykh, E. Chojnacki, Z. Conway, V. Medjidzade, H. Padamsee, P. Quigley, J. Sears, V. Shemelin, and V. Veshcherevich, SRF experience with the Cornell high-current ERL injector prototype, in *Proceedings of the 23rd Particle Accelerator Conference, Vancouver, Canada, 2009* (IEEE, Piscataway, NJ, 2009) p. TU3RAI01.